

# Reconstruction-Based 2DPCANet for Unsupervised SAR Image Change Detection

Jie Wu<sup>1</sup>, *Member, IEEE*, Qimeng Zhang, Rongrong Li, Luis Gomez<sup>2</sup>, *Senior Member, IEEE*,  
and Alejandro C. Frery<sup>3</sup>, *Fellow, IEEE*

**Abstract**—In this letter, considering the effectiveness of 2-D principal component analysis (2DPCA) on the exploration of local spatial relationships, a reconstruction-based 2DPCA (Rec-2DPCA) operation was designed for feature extraction and injected into the architecture of PCANet for change detection of bitemporal synthetic aperture radar (SAR) image. Specifically, as the projection of an image patch on one eigenvector computed by 2DPCA breaks the one-to-one relationship between feature map and eigenvalue, we adopted Rec-2DPCA at various network layers and developed two variants of PCANet, namely, 2DPCANet and (2-D + 1-D)PCANet. In the experiments, using three real SAR image datasets, we analyzed the performance of all comparison methods, and our proposals achieved a more appealing performance than other methods.

**Index Terms**—2-D principal component analysis (2DPCA), reconstruction-based 2DPCA (Rec-2DPCA), synthetic aperture radar (SAR) imagery, unsupervised change detection, vertical 2DPCA.

## I. INTRODUCTION

**D**UE to the usage of microwave in synthetic aperture radar (SAR), SAR system can capture scene's information under all-weather and all-day [1], and SAR image has been widely applied to analyze the land-cover information [2]. Moreover, with the development of SAR technology, continuous monitoring of land-cover's temporal changes with SAR image has attracted many scholars' attention [3], [4], [5], [6], [7], [8]. Specifically, by comparing at least two SAR images acquired on the same scene at different times, it points to alterations that may require further actions [2].

Given the complicated backscattering behaviors, the superimposition of speckles, and a higher labor cost on samples' annotation in SAR imagery, building an effective unsupervised feature representation model to identify the changed and

nonchanged regions within bitemporal SAR images is still a hot spot to be studied. In the literature, using Gabor features extracted from the difference images between bitemporal SAR images, Li et al. [3] proposed a two-stage fuzzy clustering-based SAR change detection method. By computing the difference features of bitemporal SAR images with Gabor filters, Yang et al. [9] adopted a multivariate Gaussian mixture model to detect changes. In [10], the log-Gabor filters were used instead of Gabor filters to compute difference features, and the K-mean method was used for change detection. Due to the orthogonality and scattering preservation property of principal component analysis (PCA), PCA-based feature was extracted in [11] for bitemporal SAR imagery change detection.

Recently, given the capability of deep neural networks (DNNs) on feature representation, some deep-learning-based SAR change detection methods have been proposed [6], [7], [8]. However, as DNNs usually contain many parameters that should be learned at the training stage [8], they always require many labeled samples and a higher time consumption for model building. In [12], inspired by the deep architecture of convolution neural network (CNN), Chen et al. proposed a two-layer PCANet for image classification, where the eigenvectors of training samples were used as convolution kernel for feature extraction at each layer while binary hashing and blockwise histogram were sequentially used for nonlinear mapping. Given the simple structure and lower time consumption in the learning stage, PCANet has been widely applied for feature extraction [13], [14], [15].

Inspired by Chan et al. [12], by stacking the paired data blocks from two registered SAR images as a sample, Gao et al. [4] designed a PCANet-based unsupervised SAR image change detection method with the help of pseudoclass labeled samples. In [16], a salient map was introduced to reduce the influence of speckle, and a saliency-guided PCANet was designed for unsupervised SAR image change detection. However, due to the vectoring of the image block to form a covariance matrix in the PCA process, the spatial relationship among pixels is usually underused [17]. By removing the vectoring operation, a 2-D PCA (2DPCA) was designed [18] for feature extraction and showed better performance on image classification than that of PCA. Thus, considering the critical role of local spatial information on feature extraction in SAR imagery [19], 2DPCA is explored, and reconstruction-based 2DPCA (Rec-2DPCA) is designed in this letter to modify PCANet for SAR image change detection. To sum up, our main contributions are listed as follows.

Received 18 December 2024; revised 9 February 2025; accepted 28 February 2025. Date of publication 4 March 2025; date of current version 21 March 2025. This work was supported in part by the Natural Science Basic Research Plan in Shaanxi Province of China under Grant 2019JQ-093 and Grant S2023-JC-QN-0762; and in part by the Consejería de Economía, Industria, Comercio y Conocimiento del Gobierno de Canarias, under Grant CEI2020-13. (*Corresponding author: Jie Wu.*)

Jie Wu and Qimeng Zhang are with the School of Computer Science, Shaanxi Normal University, Xi'an 710119, China (e-mail: 607wujie2005@163.com).

Rongrong Li is with the School of Computer Engineering, Xi'an Vocational University of Information, Xi'an 710125, China.

Luis Gomez is with the Imaging Technology Center (CTIM), Department of Electronic Engineering and Automatic Control, Universidad de Las Palmas de Gran Canaria, 35001 Las Palmas de Gran Canaria, Spain.

Alejandro C. Frery is with the School of Mathematics and Statistics, Victoria University of Wellington, Wellington 6012, New Zealand.

Digital Object Identifier 10.1109/LGRS.2025.3547844

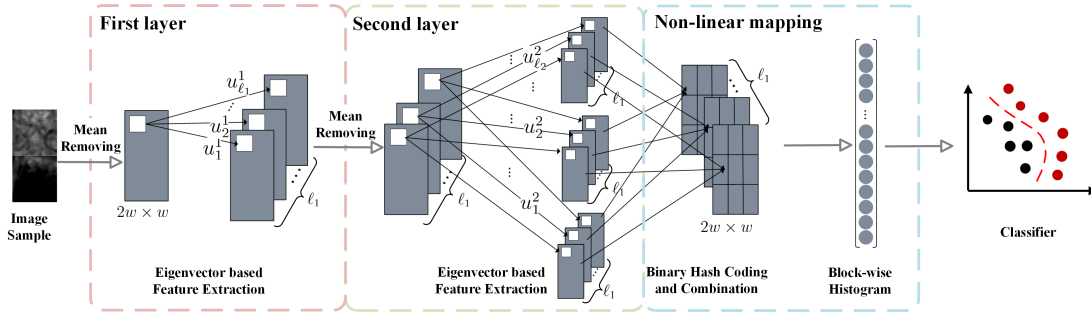


Fig. 1. Architecture of our method. Here, the image sample's size is  $2w \times w$ ,  $u_t^i$  is the  $t$ th projection vector at the  $i$ th layer, and  $l_i$  is the number of projection vectors at the  $i$ th layer.

- 1) Using Rec-2DPCA, two variants of PCANet, 2DPCANet and (2-D + 1-D) PCANet, are proposed for unsupervised SAR image change detection.
- 2) The performances of our proposals are analyzed with three real SAR image datasets, including the parameters' influence.

## II. METHODOLOGY

In this section, using the architecture shown in Fig. 1, three main processes adopted in our method are first introduced: generation of pseudoclass labels, Rec-2DPCA-based feature extraction, and nonlinear mapping. Then, the main steps of our method are given in detail.

### A. Generation of Pseudoclass Labels

In our method, Gabor features are first extracted at multi-orientation (e.g., 8) and multiscale (e.g., 5) for each pixel of the difference image  $\mathbf{DI}$  that is calculated as

$$\mathbf{DI} = \left| \log \frac{\mathbf{I}_1 + \epsilon}{\mathbf{I}_2 + \epsilon} \right| \quad (1)$$

where  $\epsilon$  is a smaller constant value, and  $\mathbf{I}_1$  and  $\mathbf{I}_2$  are two registered SAR images (intensity or amplitude) obtained at times  $t_1$  and  $t_2$ , respectively.

Then, the maximum response map among eight orientations is calculated for each scale as the final feature. With the final features, all the pixels are assigned with a pseudoclass label [i.e., changed ( $w_c$ ), unchanged ( $w_{uc}$ ), and uncertain ( $w_u$ )] via FCM clustering method embedded with a coarse to fine scheme [4].

### B. Rec-2DPCA-Based Feature Extraction

By considering the local spatial relationship in images  $\mathbf{A}_i \in \mathcal{R}^{m \times n}$ ,  $i \in \{1, \dots, N\}$ , 2DPCA was designed in [18] for feature extraction. Specifically, using the covariance matrix  $\mathbf{C} = \sum_{i=1}^N \mathbf{A}_i \mathbf{A}_i^T$ , the projection vectors are computed as

$$\arg \max_{u_k, k \in [1, q]} \mathbf{U}^T \mathbf{C} \mathbf{U} \quad (2)$$

where  $\mathbf{U} = \{u_k | k \in [1, q]\}$ ,  $u_k \in \mathcal{R}^m$  is the projection vector for all the columns of  $\mathbf{A}_i$  and satisfies  $u_a^T u_b = 0$ ,  $u_a^T u_a = 1$ ,  $a \neq b$ ,  $a, b \in [1, q]$ . Then using  $u_k$ , the feature obtained for the image sample  $\mathbf{A}_i$  is computed as  $f_k^i = \mathbf{A}_i^T u_k$ ,  $k \in [1, q]$ . Obviously,  $f_k^i \in \mathcal{R}^n$  is the vector while a scalar value is obtained by classical PCA-based projection for each sample.

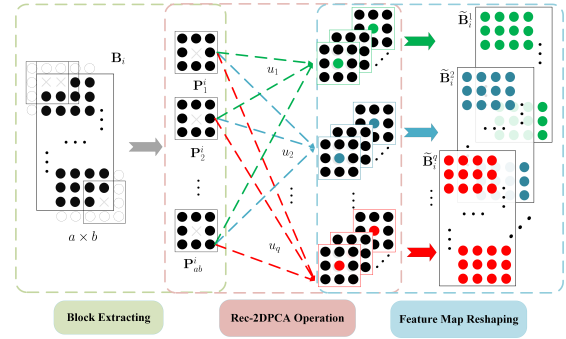


Fig. 2. Procedure of Rec-2DPCA.

In [4] and [12], using the eigenvectors corresponding to the largest  $q$  eigenvalues computed by PCA method, each input image sample was represented as  $q$  feature maps which were of the same size as that of the input sample. The procedure is similar to the convolution operator in CNN [14], [20]. And a one-to-one relationship exists between the feature maps and eigenvectors. However, using the projection vector computed by (2), the one-to-one relationship between the feature map and eigenvector is broken. Thus, to retain the relationship, the reconstruction operator is adopted and named as Rec-2DPCA to compute the feature map.

Let  $\mathbf{B}_k \in \mathcal{R}^{a \times b}$ ,  $k \in \{1, \dots, N\}$  be the image sample, the procedure of Rec-2DPCA (shown in Fig. 2) is described as follows.

- 1) Centering on each pixel of  $\mathbf{B}_k$ , a set of patches (e.g.,  $\mathbf{P}_t^k \in \mathcal{R}^{s_1 \times s_2}$ ,  $t \in \{1, \dots, ab\}$ ) are extracted.
- 2) For all the image samples, mean-removed patches are computed by  $\hat{\mathbf{P}}_t^k = \mathbf{P}_t^k - \bar{\mathbf{P}}^k$ . Here,  $\bar{\mathbf{P}}^k = (1/ab) \sum_{t=1}^{ab} \mathbf{P}_t^k$ .
- 3) Using mean-removed patches, the covariance matrix is computed as  $\mathbf{C} = \sum_{k=1}^N \sum_{t=1}^{ab} \hat{\mathbf{P}}_t^k \hat{\mathbf{P}}_t^{kT}$ .
- 4) By solving (2), the eigenvectors of  $\mathbf{C}$ , corresponding to first  $q$  largest eigenvalues, are stored as  $\mathbf{U} = [u_1, u_2, \dots, u_q]$  and  $u_j \in \mathcal{R}^{s_1}$ ,  $j \in \{1, \dots, q\}$ .
- 5) Computing the feature map of  $\mathbf{B}_k$  with  $u_j$  as

$$\tilde{\mathbf{B}}_k^j = \text{Mat}([\text{Cp}(u_j u_j^T \mathbf{P}_1^k), \dots, \text{Cp}(u_j u_j^T \mathbf{P}_T^k)])$$

where  $\text{Cp}(\cdot)$  is the operator extracting the center point's value and  $\text{Mat}(\cdot)$  indicates the reshape operation.

It is clear that  $\tilde{\mathbf{B}}_k^j$  is of the same size as that of  $\mathbf{B}_k$  and is of the one-to-one relationship with  $u_j$  for  $\mathbf{B}_k$ .

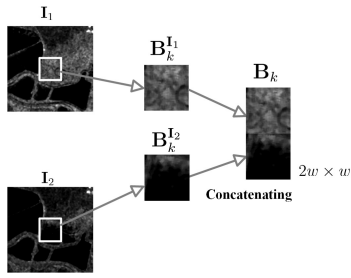


Fig. 3. Generation of image sample via concatenation.

### C. Nonlinear Mapping

As nonlinear mapping is beneficial to the performance of PCANet [4], [12], this process is also used in our method. Specifically, using two-layer architecture shown in Fig. 1 and assuming the number of used eigenvectors is  $\ell_i, i \in \{1, 2\}$  at the  $i$ th layer, all the output maps corresponding to the same input at the second layer are binarized to form integer map  $\mathbf{Z}^j, j \in \{1, \dots, \ell_1\}$  whose  $k$ th pixel's value is computed as

$$z_k = \sum_{l=1}^{\ell_2} 2^{\ell_2-l} \times H(x_k^l) \quad (3)$$

where  $H(x) = 0$  if  $x < 0$ , otherwise  $H(x) = 1$ , and  $x_k^l$  is the value of the  $k$ th pixel at the  $l$ th output map in the second layer.

Then, the obtained integer maps are divided into  $d$  blocks, and the features of an image sample are computed as

$$f = \left[ \text{hist}(\mathbf{Z}_1^1), \dots, \text{hist}(\mathbf{Z}_d^1), \dots, \text{hist}(\mathbf{Z}_d^{\ell_1}) \right] \in \mathcal{R}^{(2^{\ell_2}) \cdot \ell_1 \cdot d}$$

where  $\mathbf{Z}_t^i$  is the  $t$ th block in the  $i$ th integer image and  $\text{hist}(\cdot)$  is the histogram operation.

Finally, given the effectiveness of support vector machine (SVM) on classification, we use SVM as a classifier to compute the final changed map.

### D. Proposed Method

Given the higher reliability of samples whose pseudoclass label is  $w_c$  and  $w_{uc}$ , we randomly selected samples from these two sample sets for model building. To sum up, the main steps of our method are described as follows.

- 1) According to Section II-A, all the samples are assigned with pseudoclass labels (i.e.,  $w_c, w_{uc}$  and  $w_u$ ).
- 2) According to the ratio between samples whose labels are  $w_c$  and  $w_{uc}$ , training set  $T$  is formed via randomly selection of these two samples.
- 3) Using the architecture shown in Fig. 1, all the samples in  $T$  are used to learn the eigenvectors as in Section II-B and the parameters of SVM.
- 4) With the learned parameters, the feature of each sample assigned as  $w_u$  is computed, and these samples are classified as  $w_c$  or  $w_{uc}$  to obtain the final changed map.

Specifically, centering on each pixel, two registered image blocks ( $w \times w$ ) are stacked as in Fig. 3 to be an image sample in our method for feature extraction at steps 3) and 4). Note that the size of the patch is set as  $p \times p$ . And, 2DPCANet and (2-D + 1-D)PCANet are designed, where Rec-2DPCA is exploited at both the layers in 2DPCANet, while only the first layer uses Rec-2DPCA in (2-D + 1-D)PCANet.

## III. RESULTS AND EXPERIMENTS

In this section, we first introduce the datasets and evaluation metrics used in the experiments. Then, we compare the visual and numerical results of all the comparison methods. Finally, some critical parameters of our proposals are analyzed.

### A. Datasets and Evaluation Metrics

To make a better analysis, we use three SAR image datasets, as follows.

- 1) Yellow River [257 × 289 pixels, shown in Fig. 4(a) and (b) (top)], acquired in 2008 and 2009 by RADARSAT-2 in the Yellow River estuary area of China. Note the image captured in 2008 is single-look, while the other one has four nominal looks.
- 2) San Francisco [256 × 256 pixels, shown in Fig. 4(a) and (b) (middle)], obtained in August 2003 and May 2004 by RADARSAT.
- 3) Ottawa [290 × 350 pixels, shown in Fig. 4(a) and (b) (bottom)], acquired on May and August 1997 by ERS-2 in the flooded area of Ottawa.

The corresponding ground-truth map is shown at each row in Fig. 4(c). Besides, we selected six well-known numerical metrics for a quantitative analysis. They are: false alarms (FAs), missed alarms (MAs), overall error (OE), accuracy (ACC), F1 score (F1), and kappa coefficient (KC).

### B. Parameter-Setting and Result Analysis

1) *Settings for 2DPCANet*: From (2), we can see that the number of feature maps is limited by the size of  $\mathbf{C}$  that is computed with image patches. Thus, we fix  $p = w = 17$ . In addition, each layer selects eigenvectors corresponding to the six largest eigenvalues for feature extraction.

2) *Settings for (2-D + 1-D)PCANet*: For (2-D + 1-D) PCANet, we fix  $w = p = 5$ . The number of eigenvectors used at the first and second levels is four and 16, respectively.

3) *Comparison Method*: We compare our proposals with CWNN [5], PCAKM [11], GaborTLC [3], and PCANet [4]. The parameter settings of all the comparison methods are set according to the literature's recommendations. Note that the difference image computed by (1) is used in all the methods.

4) *Result Analysis*: In Fig. 4, the visual results of all the comparison methods on three SAR datasets are given. For a better visual analysis, we combined the ground-truth map and the results obtained by different approaches to form RGB images in Fig. 4(d)–(i) where red color pixels imply the FA sample obtained by the method and pixels with green color indicates the method's MA sample. In addition, the regions marked in the blue box for 2DPCANet and (2-D + 1-D) PCANet are cropped and enlarged in Fig. 4(h) and (i).

In Table I, the numerical indices are computed and listed. Here, we report the median over ten independent replications using 30% randomly selected samples assigned with  $w_c$  and  $w_{uc}$  for training. The best values are marked in bold, while the second best are underlined.

From Fig. 4, we see that our methods reduce the number of FA samples compared with CWNN and PCAKM in the unchanged regions, except the area near the boundary of changed regions. The result can be found in Table I, where (2-D + 1-D)PCANet consistently achieves a lower FA and OE

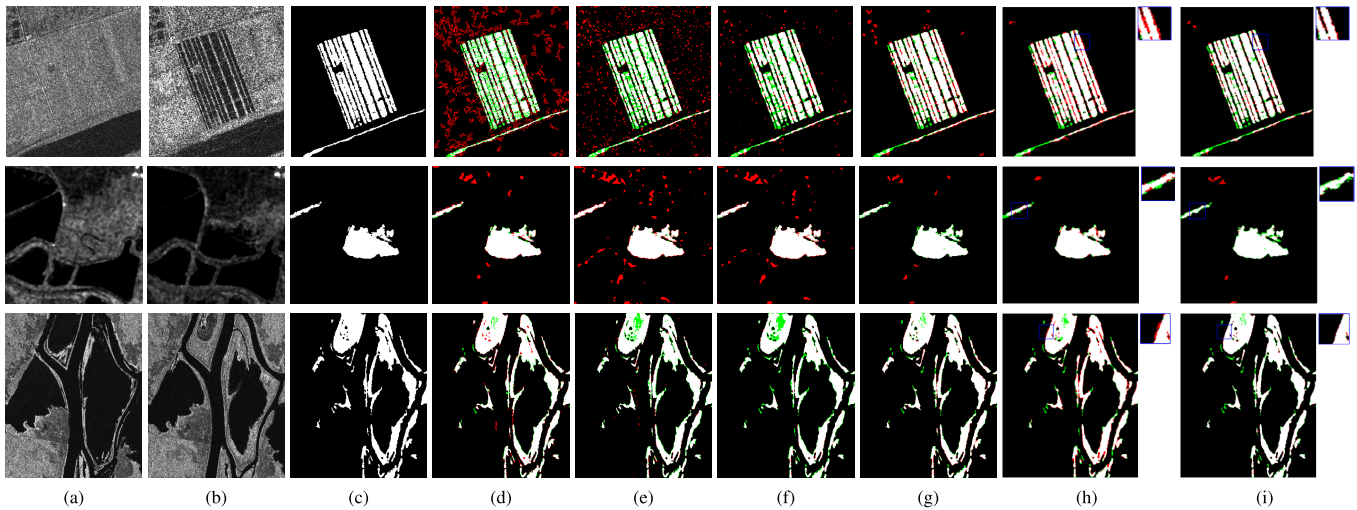


Fig. 4. (From top to bottom) Results on the Yellow River, San Francisco, and Ottawa datasets. (a) and (b) SAR images. (c) Ground-truth maps. (d) CWNN. (e) PCAKM. (f) GaborTLC. (g) PCANet. (h) 2DPCANet. (i) (2-D + 1-D)PCANet. Changed and unchanged regions are in white and black, respectively. FA sample appears in red, and the MA sample is in green.

TABLE I  
PERFORMANCE METRICS OBTAINED BY DIFFERENT METHODS ON REAL SAR IMAGE DATASETS

Method	YellowRiver						San Francisco						Ottawa					
	FA	MA	OE	ACC(%)	F1(%)	KC(%)	FA	MA	OE	ACC(%)	F1(%)	KC(%)	FA	MA	OE	ACC(%)	F1(%)	KC(%)
CWNN [5]	7130	3591	10721	86.23	71.48	62.50	767	203	970	98.52	90.62	89.82	1173	<b>1003</b>	2176	97.88	93.65	92.38
PCAKM [11]	4188	3371	7559	90.26	78.04	71.79	2033	<u>72</u>	2105	96.79	81.66	79.95	578	1902	2480	97.60	92.83	91.39
GaborTLC [3]	<u>1656</u>	2869	4525	94.13	85.58	81.91	1376	<b>60</b>	1436	97.81	86.71	85.54	<b>253</b>	2531	2784	97.32	92.02	90.42
PCANet [4]	2240	<u>1654</u>	3894	94.87	87.34	84.13	331	352	<b>683</b>	98.96	<u>93.21</u>	92.64	847	<u>1184</u>	<u>2031</u>	<u>98.02</u>	<u>94.05</u>	<u>92.86</u>
<b>2DPCANet</b>	2341	<b>1357</b>	3698	<u>95.11</u>	<u>87.90</u>	<u>84.84</u>	<b>275</b>	304	<b>579</b>	<b>99.12</b>	<b>94.18</b>	<b>93.70</b>	1893	1370	3263	96.83	90.77	88.86
<b>(2D+1D)PCANet</b>	<b>1439</b>	1760	<b>3199</b>	<b>95.79</b>	<b>89.36</b>	<b>86.74</b>	<u>316</u>	423	739	98.88	92.69	92.08	<u>507</u>	1342	<b>1849</b>	<b>98.20</b>	<b>94.55</b>	<b>93.48</b>

TABLE II  
RATIO OF MISS-CLASSIFIED PIXELS NEAR THE  
BOUNDARY OF REAL CHANGED REGIONS

Method	YellowRiver	San Francisco	Ottawa
2DPCANet	<b>0.8598</b>	<b>0.8159</b>	0.8779
(2D+1D)PCANet	0.8500	0.6411	<b>0.8990</b>

than that of CWNN and PCAKM. Besides, the values of FA obtained by (2-D + 1-D)PCANet are consistently lower than those achieved by PCANet. The main reason is spatial information is considered in our methods for feature extraction. For San Francisco, the visual comparison among GaborTLC, PCANet, and 2DPCANet reveals that the FA samples are significantly reduced in unchanged area by 2DPCANet [shown as the second row in Fig. 4(f)–(h)]. The result can also be obtained from Table I where 2DPCANet achieves the best performance in terms of OE, ACC, F1, and KC, while the performance of (2-D + 1-D)PCANet is comparable with that of PCANet whose performance is only inferior to that of 2DPCANet. For Yellow River and Ottawa, the best performance is always obtained by (2-D + 1-D)PCANet in terms of OE, ACC, F1, and KC. The main reason is (2-D + 1-D)PCANet stacked Rec-2DPCA and 1DPCA for feature representation. By comparing the results of (2-D + 1-D)PCANet and 2DPCANet, we find that FA and MA samples are mainly located at the boundary of the anisotropic changed region for 2DPCANet [shown as the enlarged area marked by the blue box in Fig. 4(h) and (i)]. The result can also be obtained from Table II where the ratio

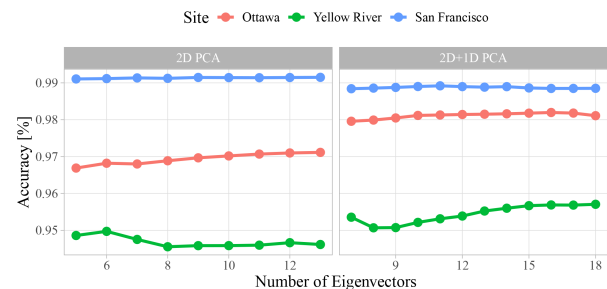


Fig. 5. Performance of (Left) 2DPCANet and (Right) (2-D + 1-D)PCANet varying the number of components.

of miss-classified pixels near the boundary of the real changed region is computed for 2DPCANet, and (2-D + 1-D)PCANet, and a large value is usually obtained by 2DPCANet. The main reason is that local complex spatial information should be carefully considered for effective image feature extraction.

### C. Parameters Analysis

As in [12], the number of eigenvectors significantly affects the network's performance. Therefore, using the parameter settings in Section III-B, the impact of the number of eigenvectors on the performance of our proposals is shown in Fig. 5.

Note that as  $p = 5$  is used for (2-D + 1-D)PCANet, only the number of eigenvectors used in the second layer is analyzed, while the numbers of eigenvectors used in both the layers of 2DPCANet are fixed as the same and adjusted in Fig. 5.

TABLE III  
RUNNING TIME OF THE TRAINING AND TESTING PHASES

Method	YellowRiver		San Francisco		Ottawa	
	Train	Test	Train	Test	Train	Test
PCANet	1733s	2500s	1442s	524s	2373s	1409s
2DPCANet	292s	179s	249s	40s	378s	100s
(2D+1D)PCANet	20s	22s	17s	5s	28s	12s

From the figure of 2DPCANet (left), we can see a slow increase in its performance for San Francisco and Ottawa, while a significant decrease is observed from 6 to 8 for Yellow River. The main reason is that the corresponding difference image contains lots of disruptions. Thus, we set the number of eigenvectors as 6 for 2DPCANet.

For (2-D + 1-D)PCANet (right), the results of Yellow River show a large increase, following a stable persistence after 15. Ottawa’s result shows a slowing increase, reaching a peak at 16. Thus, we set the number of eigenvectors at the second layer of (2-D + 1-D)PCA to 16.

D. Computational Complexity

According to Section II-D, the covariance matrix  $C \in \mathcal{R}^{p \times p}$  is used for Rec-2DPCA, while  $C \in \mathcal{R}^{2p \times 2p}$  for PCA. Assuming  $N$  is the number of image samples and  $\ell$  is the number of selected eigenvectors, the computational complexity of the Rec-2DPCA-based feature extraction method is calculated as  $O(Nw^2(2p^3 + 3p^2 + (2p + 1)\ell) + p^3 + p^2)$ . At the same time, it is  $O(2Nw^2(p^4 + p^2(\ell + 1)) + p^2 + p^6)$  for the PCA-based method. As  $Nw^2 \gg p^2 > \ell$ , the complexity of the Rec-2DPCA-based method is lower than that of the PCA-based approach. This can also be obtained from Table III where the running times (unit: seconds) are calculated using MATLAB under CentOS 7.0 (Intel Xeon 6254 CPU, 3.1 GHz) and 40-GB RAM. Obviously, the lowest running time is always achieved by (2-D + 1-D)PCANet where the size of the image block used for feature extraction is comparable with that of PCANet, while a larger image block is adopted in 2DPCANet.

IV. CONCLUSION

In this letter, considering the effectiveness of spatial information on speckled image processing, Rec-2DPCA was designed for unsupervised change detection of SAR imagery, with which we designed two variants of PCANet, namely, (2-D + 1-D)PCANet and 2DPCANet.

We assessed the performance of these two methods with three real SAR datasets and verified that the contextual information improved the results. From the comparison and analysis, we can see that due to the usage of Rec-2DPCA, the designed method achieved good detection results, especially in suppressing the FAs in the larger unchanged area.

As Rec-2DPCA was used for feature extraction, each input image is represented in the image domain. Thus, other representations, e.g., in extracted feature domains, will be studied.

ACKNOWLEDGMENT

The authors would like to thank Prof. Gao Feng for sharing real SAR imagery and the code of PCANet. They also greatly appreciate the reviewers’ suggestions and the editor’s encouragement.

REFERENCES

- [1] B. Cui et al., “Enhanced edge information and prototype constrained clustering for SAR change detection,” *IEEE Trans. Geosci. Remote Sens.*, vol. 62, pp. 1–16, 2024, Art. no. 5206116.
- [2] V. Macchiarulo, G. Giardina, P. Milillo, Y. D. Aktas, and M. R. Z. Whitworth, “Integrating post-event very high resolution SAR imagery and machine learning for building-level earthquake damage assessment,” *Bull. Earthq. Eng.*, Mar. 2024, doi: 10.1007/s10518-024-01877-1.
- [3] H.-C. Li, T. Celik, N. Longbotham, and W. J. Emery, “Gabor feature based unsupervised change detection of multitemporal SAR images based on two-level clustering,” *IEEE Geosci. Remote Sens. Lett.*, vol. 12, no. 12, pp. 2458–2462, Dec. 2015.
- [4] F. Gao, J. Dong, B. Li, and Q. Xu, “Automatic change detection in synthetic aperture radar images based on PCANet,” *IEEE Geosci. Remote Sens. Lett.*, vol. 13, no. 12, pp. 1792–1796, Dec. 2016.
- [5] F. Gao, X. Wang, Y. Gao, J. Dong, and S. Wang, “Sea ice change detection in SAR images based on convolutional-wavelet neural networks,” *IEEE Geosci. Remote Sens. Lett.*, vol. 16, no. 8, pp. 1240–1244, Aug. 2019.
- [6] Y. Li, C. Peng, Y. Chen, L. Jiao, L. Zhou, and R. Shang, “A deep learning method for change detection in synthetic aperture radar images,” *IEEE Trans. Geosci. Remote Sens.*, vol. 57, no. 8, pp. 5751–5763, Aug. 2019.
- [7] S. Chen, X. Su, L. Zheng, and Q. Yuan, “Statistic ratio attention-guided Siamese U-Net for SAR image semantic change detection,” *IEEE Geosci. Remote Sens. Lett.*, vol. 21, pp. 1–5, 2024.
- [8] Y. Duan et al., “WCMU-net: An effective method for reducing the impact of speckle noise in SAR image change detection,” *IEEE J. Sel. Topics Appl. Earth Observ. Remote Sens.*, vol. 18, pp. 2880–2892, 2025.
- [9] G. Yang, H.-C. Li, W. Yang, K. Fu, Y.-J. Sun, and W. J. Emery, “Unsupervised change detection of SAR images based on variational multivariate Gaussian mixture model and Shannon entropy,” *IEEE Geosci. Remote Sens. Lett.*, vol. 16, no. 5, pp. 826–830, May 2019.
- [10] R. V. Geetha and S. Kalaivani, “A feature based change detection approach using multi-scale orientation for multi-temporal SAR images,” *Eur. J. Remote Sens.*, vol. 54, no. 2, pp. 248–264, 2021.
- [11] T. Celik, “Unsupervised change detection in satellite images using principal component analysis and  $k$ -means clustering,” *IEEE Geosci. Remote Sens. Lett.*, vol. 6, no. 4, pp. 772–776, Oct. 2009.
- [12] T.-H. Chan, K. Jia, S. Gao, J. Lu, Z. Zeng, and Y. Ma, “PCANet: A simple deep learning baseline for image classification?” *IEEE Trans. Image Process.*, vol. 24, no. 12, pp. 5017–5032, Dec. 2015.
- [13] P. Zhang et al., “High-order triplet CRF-PCANet for unsupervised segmentation of nonstationary SAR image,” *IEEE Trans. Geosci. Remote Sens.*, vol. 59, no. 10, pp. 8433–8454, Oct. 2021.
- [14] S. Li, Y. Zou, G. Wang, and C. Lin, “Infrared and visible image fusion method based on a principal component analysis network and image pyramid,” *Remote Sens.*, vol. 15, no. 3, p. 685, Jan. 2023.
- [15] M. Yang, J. Yang, H. Mao, and C. Zheng, “Damage scene change detection based on infrared polarization imaging and fast-PCANet,” *Remote Sens.*, vol. 16, no. 19, p. 3559, Sep. 2024.
- [16] M. Li, M. Li, P. Zhang, Y. Wu, W. Song, and L. An, “SAR image change detection using PCANet guided by saliency detection,” *IEEE Geosci. Remote Sens. Lett.*, vol. 16, no. 3, pp. 402–406, Mar. 2019.
- [17] Z. Li, L. Yao, S. Wang, S. S. Kanhere, X. Li, and H. Zhang, “Adaptive two-dimensional embedded image clustering,” in *Proc. AAAI Conf. Artif. Intell.*, Apr. 2020, vol. 34, no. 4, pp. 4796–4803.
- [18] J. Yang, D. Zhang, A. F. Frangi, and J.-Y. Yang, “Two-dimensional PCA: A new approach to appearance-based face representation and recognition,” *IEEE Trans. Pattern Anal. Mach. Intell.*, vol. 26, no. 1, pp. 131–137, Jan. 2004.
- [19] J. Wu, F. Liu, H. Hao, L. Li, L. Jiao, and X. Zhang, “A nonlocal means for speckle reduction of SAR image with multiscale-fusion-based steerable kernel function,” *IEEE Geosci. Remote Sens. Lett.*, vol. 13, no. 11, pp. 1646–1650, Nov. 2016.
- [20] J. Yu and J. Liu, “Two-dimensional principal component analysis-based convolutional autoencoder for wafer map defect detection,” *IEEE Trans. Ind. Electron.*, vol. 68, no. 9, pp. 8789–8797, Sep. 2021.